Fully Nonlinear Time Domain Analysis for Hydrodynamic Performance of an Oscillating Wave Surge Converter

SUN Shi-yan[a], SUN Shi-li[b], WU Guo-xiong[a,c*]

[a] School of Naval Architecture & Ocean Engineering, Jiangsu University of Science and Technology, Zhenjiang 212003, China

[b] College of Shipbuilding Engineering, Harbin Engineering University, Harbin 150001, China

[c] Department of Mechanical Engineering, University College London, Torrington Place, London WC1E 7JE, UK

Abstract

The hydrodynamic behaviour of an oscillating wave surge converter (OWSC) in large motion excited by nonlinear waves is investigated. The mechanism through which the wave energy is absorbed in the nonlinear system is analysed. The mathematical model used is based on the velocity potential theory together with the fully nonlinear boundary conditions on the moving body surface and deforming free surface. The problem is solved by the boundary element method. Numerical results are obtained to show how to adjust the mechanical properties of the OWSC to achieve the best efficiency in a given wave, together with the nonlinear effect of the wave height. Numerical results are also provided to show the behaviour of a given OWSC in waves of different frequencies and different heights.

Keywords: Wave energy, Oscillating wave surge converter, Nonlinear wave/structure interactions, Boundary element method.

1 Introduction

With the extensive use of fossil energy, it becomes evident that this is not sustainable as the energy resource can be exhausted. Furthermore the excessive use of this kind of energy has caused environment pollution and climate change. Therefore there has been an increasing interest in developing technology to efficiently make use of renewable energy, in the form of water wave, hydro, wind and solar powers, *etc*. Indeed some of technologies are already widely in use, and had supplied an estimated 22.1% of global electricity consumption by the end of 2013, among which hydropower provided about 16.4%, and wind energy produced around 2.9%. In contrast, use of wave energy is less developed while it has a great potential.

Most wave energy exits in deep seas, and thus the earlier wave energy converters were usually designed for deeper waters (Salter, 1974, Budal and Falnes, 1975&1978, Evans, 1976&1981). While during recent years, the wave energy in nearshore has received increasing attentions, which is a result of the new understanding of the nature of wave energy. It is common that the nearshore wave power resource is dramatically less than that offshore. However this statement is usually based on the omni-directional or gross wave power resource, which is particularly advantageous for the devices which are not sensitive to the direction of wave propagation such as isolated axi-symmetric heaving buoys. However for the devices which respond differently to waves from different directions, “the exploitable wave energy resource”, which is defined as the mean value of the directionally resolved incident wave power, where the threshold power level is not allowed to be more than four times the mean value, is a more realistic measure (Folley and Whittaker, 2009). Based on such a new definition, there is only 10–20% energy losses from the offshore to the

*Corresponding author. E-mail: g.wu@ucl.ac.uk

nearshore in many sea sites (Folley et al., 2009). From engineering and economy perspectives, the devices located in the nearshore have a number of advantages. Through the depth induced wave breaking, the large although infrequent extreme waves, which may be a threat to the survival of wave energy devices, can be filtered (Henry et al., 2014). In addition, cost of the cables which are used to bring power to the shore and power losses in the cables will be lower due to closer distance to the coast. The installation and maintenance costs in nearshore are likely to be reduced due to the shorter weather windows, the closer location to the shoreline and shallow water depth (Folley et al., 2007a). Thus the wave energy converters designed for shallower water gradually gain momentum during the last decade. This type of devices are often classified as oscillating wave surge converters (OWSCs), as energy is mainly extracted from the horizontal or surging motion of water particles in ocean waves (Whittaker and Folley, 2012). One of the most typical OWSCs is Oyster. This device is a buoyant and hinged flap which is attached to the seabed and has the top edge piercing through the water surface. It is usually used in area of water depth of between 10 and 15 m, which is often referred to as nearshore. Two full-scale prototypes of Oyster were installed in summers of 2009 and 2011 at the European Marine Energy Centre's test site (EMEC), Orkney, Scotland. Apart from Oyster, WaveRoller (Folley et al., 2007b) with a flap completely submerged is another typical representative of OWSCs. The previous two devices typically comprise a single flap spanning their full width. Recently, a new concept 'Modular Flap', formed by splitting the flap into multiple modules, is receiving increasing attention. Sarkar et al. (2016) made comparison of the performances between a rigid flap and a modular system with six identical modules. The combined length of the latter was the same as that of the former. It was found that the module system had the potential to gain more energy due to its multiple natural frequencies at which resonance could occur. Wilkinson et al. (2017) showed through both the numerical and experimental methods that the modular device could absorb power more smoothly.

Over the past decade, OWSCs have been investigated by many authors though various analytical and numerical methods. Folley et al. (2005, 2007a) investigated the effect of water depth on the power capture efficiency and surge wave force of an OWSC through the combined method of analytical and numerical results. The capture efficiency and surge wave force were obtained through the equations with hydrodynamic coefficients obtained from the linear potential flow theory. Similar work includes those by Folley et al. (2007b), Van't Hoff (2009), and Whittaker and Folley (2012). In addition, a three dimensional semi-analytical model based on the potential flow theory was developed by Renzi and Dias (2012a, 2012b, 2013) to investigate the behaviour of an OWSC. Recent years, generally CFD techniques have been increasingly used. Among them, Smoother particle hydrodynamics (SPH) method was used by Rafiee et al. (2013) to investigate the wave loading on an OWSC, and by Yeylaghi et al. (2016) to investigate the interaction between wave and OWSC. Another important CFD technique is to combine the finite volume method (FVM) in solving RANS function, with some surface tracking methods, such as volume of fluid (VOF) or level-set (LS) technique for the free surface. In this context, viscous effects and slamming effects on an OWSC were investigated by Wei *et al.* (2015, 2016) though the Fluent Software. Similar method was also adopted by Schmitt and Elsaesser (2015) in simulating the motion of an OWSC in significant waves through an open source toolbox OpenFOAM.

Within the linear theory, it is generally accepted that the wave energy absorbed by WECs from waves very much depends on the difference between the wave and body frequencies and the damping from the power take-off system. Specifically, the wave energy converter must

first be resonated at the design wave frequency. Simultaneously, the radiation damping of the WEC should be matched with the externally imposed damping. Mei (2012) named it as "impedance matching", and found that the power output could be maximized when "impedance matching" was realized. Therefore achieving resonances is recognized as one of the best options to improve the performance of a WEC. For instance, a coupled resonance was considered by Evans and Porter (2012) through inserting a water tank having separate mass /spring /damper characteristics into a WEC. The multiple resonances of system were exploited by Crowley et al. (2013) through inserting a mechanical system of compound pendulums inside the hollow cylinder to provide a broad-banded response. Other similar work includes those by Eriksson et al. (2005) and Renzi and Dias (2012a, 2012b, 2013).

Within the potential theory, the linear frequency domain method, which is most commonly used above, is very effective for the efficiency evaluation of WECs in small regular waves. However, in large waves, the neglected nonlinear effects may lead to the significant deviation of the efficiency and performance evaluation. In such a case the fully nonlinear time domain method may be needed. In the present paper, we shall focus on the oscillating wave surge converter undergoing large amplitude motion. The governing Laplace equation will be solved by the boundary element method (BEM). The nonlinear free surface boundary conditions will be satisfied through time stepping method. In the following sections, we shall first introduce briefly the OWSC system, with the definitions and equations for the absorbed power and efficiency. This is followed by the detailed description and the methodology for hydrodynamic analysis. Results are then provided to assess the performance of the device in the nonlinear periodic waves. Efficiency analysis is undertaken in a given incoming wave while varying the natural frequency and the mechanical damping of the system. Analysis is also made to access the nonlinear effect through the incoming wave amplitude. All these aim to provide a better understanding of the mechanism of wave energy conversion.

2 Methodology for efficiency prediction

2.1 Definition of wave energy absorbing efficiency of an oscillating wave surge converter

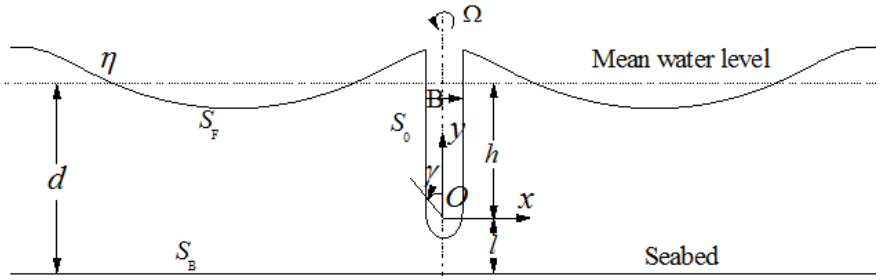

Fig. 1. The sketch of an oscillating wave surge converter

From a practical point of view, OWSC is a three dimensional device. However two dimensional analysis can still shed some insight into the physics of the problem. Fig. 1 gives a sketch of a two dimensional OWSC (Henry et al., 2014), in which a flap hinged at distance h from the calm water surface, is allowed to rotate about a horizontal axis perpendicular to the direction of wave propagation. The Cartesian coordinate system $O-xy$ with the origin O fixed at the hinge centre is defined so that x axis is parallel to the flat seabed with depth d and y axis points vertically upwards. The angular displacement γ is zero when the flap is in the vertical position and is positive in the anticlockwise direction. Ω is the angular velocity and therefore $\Omega = d\gamma / dt$. In

the present paper, the distance h, the acceleration due to gravity g, and the water density ρ are used for dimensionalisation. The flap will be in oscillatory rotation under the excitation of the wave, and its hydrodynamic behaviour is to be investigated through the time stepping method. It is expected that the rotation of the flap is resisted by the forces exerted by the generator. Thus the equation of motion of the flap can be written as

$$(I + a_{\text{pto}})\dot{\Omega} + b_{\text{pto}}\Omega + c_{\text{pto}}\gamma = M \tag{1}$$

where dot denotes temporal derivative, I is the rotational inertia of the flap about the hinge, a_{pto} and c_{pto} respectively imply the inertia and elastic characteristic of the generator, while b_{pto} implies the mechanical damping due to power take off system or generator. M in Eq. (1) is the moment due to fluid as well as the gravity. The power per unit length E_{P} extracted by the converter over each cycle is the average of the work done to the converter by the fluid over a period of time. We have

$$E_{\text{P}} = \frac{1}{mT}\int_{t}^{t+mT} M\Omega dt = \frac{b_{\text{pto}}}{mT}\int_{t}^{t+mT} \Omega^2 dt \tag{2}$$

after Eq.(1) is used to obtain M and the coefficients are assumed to be as constants, where T is the period of the body motion and $m \geq 1$ is an integer. If we write

$$\gamma = \text{Re}(\sum_{\text{n}=0}^{\infty} \theta_{\text{n}} e^{-in\omega t}) \tag{3}$$

where $\omega = T/2\pi$ is the frequency and θ_n is the complex amplitude corresponding to the oscillation at the frequency $n\omega$, then Eq. (2) becomes

$$E_{\text{P}} = \frac{1}{2} b_{\text{pto}} \omega^2 \sum_{n=1}^{\infty} (n|\theta_{\text{n}}|)^2 \tag{4}$$

which shows that b_{pto} is the equivalent energy extraction rate.

To consider efficiency of the device, we may consider the energy propagation in the incident wave. If the wave energy E confined within $0 < x < \lambda$, where λ is the wavelength, we then have (Wehausen and Laitone, 1960)

$$\frac{dE}{dt} = \int_{-l}^{\eta(\lambda,t)} \varphi_t \varphi_x dy - \int_{-l}^{\eta(0,t)} \varphi_t \varphi_x dy \tag{5}$$

The first term is in fact the energy leaving the domain and the second term is the energy moving into the domain and is the one to be absorbed. We notice that for the progressing wave, $\varphi(x,y,t) = \varphi(x-ct,y)$, where $c = \omega/k$ is the speed of the wave and k is the wave number. This gives $\varphi_t = -c\varphi_x$. Thus, the average energy flux over a period at $x = 0$ becomes

$$E_{\mathrm{W}} = \frac{\lambda}{T^2}\int_0^T \int_{-l}^{\eta(0,t)} \varphi_x^2 dydt \tag{6}$$

in which $\lambda = cT$ has been used and η is the elevation of the free surface. The efficiency R of the system can be defined as the ratio of the power extracted by the device to the power in the incident wave, or

$$R = \frac{E_{\mathrm{P}}}{E_{\mathrm{W}}} \tag{7}$$

2.2 Hydrodynamic analysis for fully nonlinear interaction between waves and converter

For the wave problem, water can be assumed to be inviscid as the viscous effect becomes important only after many wave periods or wavelengths (Lighthill, 1978). When the fluid is further assumed to be incompressible and the flow to be irrotational, the velocity potential whose gradient is equal to the fluid velocity can be introduced and it satisfies the Laplace equation. Let the incident potential be denoted by φ_{I} and the incident wave elevation by η_{I}. Eq. (6) becomes

$$E_{\mathrm{W}} = \frac{\lambda}{T^2}\int_0^T \int_{-l}^{\eta_{\mathrm{I}}(0,t)} \varphi_{\mathrm{I}x}^2 dydt \tag{8}$$

In addition to the incident wave, the moment M in Eqs. (1) and (2) includes the contribution from the diffracted and radiated waves. This can be obtained only by solving the hydrodynamic problem. Based on the velocity potential theory, the total potential φ, including incident, diffracted and the radiated waves, satisfies the Laplace equation in the fluid domain

$$\nabla^2 \varphi = 0 \tag{9}$$

Based on the impermeable body surface boundary condition, the normal derivative of the potential can be written as

$$\frac{\partial \varphi}{\partial n} = \Omega \cdot (x n_y - y n_x), \quad \text{on} \quad S_0 \tag{10}$$

where $\mathbf{n} = (n_x, n_y)$ is the normal of the body surface pointing out of the fluid domain. Similar impermeable boundary condition can be imposed on the fixed bottom of the fluid. Thus we have

$$\frac{\partial \varphi}{\partial n} = 0, \quad \text{on} \quad S_{\mathrm{B}} \tag{11}$$

The dynamic and kinematic boundary conditions on the free surface S_{F} in the Lagrangian form can respectively be written as

$$\frac{D\varphi}{Dt} = \frac{1}{2}\nabla\varphi \cdot \nabla\varphi - \eta \tag{12}$$

$$\frac{Dx}{Dt} = \frac{\partial \varphi}{\partial x}, \quad \frac{Dy}{Dt} = \frac{\partial \varphi}{\partial y} \tag{13}$$

At the far field, the disturbed wave will propagate to infinity and there should be no reflection. Numerically, the disturbed wave will be absorbed and then diminishes when $|x| \to \infty$. In such a

case, the potential will tend to the incident potential, or

$$\frac{\partial \varphi}{\partial n} = \frac{\partial \varphi_{\mathrm{I}}}{\partial n}, \quad |x| \to \infty \tag{14}$$

To implement in the numerical simulation, this condition is imposed at a truncated vertical boundary at a sufficiently large distance $|x|$. On the free surface near the truncated boundary, a numerical damping zone, is introduced in the dynamic and kinematic free boundary conditions in the following mixed-Eulerian-Lagrangian (MEL) form (Contento et al., 2001, Aliabadi et al., 2013)

$$\frac{\delta \varphi}{\delta t} = -\frac{1}{2}\nabla\varphi \cdot \nabla\varphi + \varphi_y \cdot (\varphi_y - \varphi_x \cdot \eta_x) - \eta - \nu(x) \cdot (\varphi - \varphi_{\mathrm{I}}) \tag{15}$$

$$\frac{\partial \eta}{\partial t} = \varphi_y - \eta_x \varphi_x - \nu(x) \cdot (\eta - \eta_{\mathrm{I}}) \tag{16}$$

where $\frac{\delta \varphi}{\delta t}$ includes the variation of the potential due to the change of the free surface elevation. We notice that the last terms in both Eqs. (15) and (16) correspond to the difference between the total potential (total wave elevation) and the incident potential (incident wave elevation). This is to ensure only the disturbed potential, including the diffracted and radiated potentials, is absorbed, but not the incident potential φ_{I}. The damping coefficient $\nu(x)$ in these two equations is chosen such a way to ensure a smooth transition from Eqs. (12) and (13) to (15) and (16) at their intersection $|x| = |x_0|$. We adopt the following form in the present work

$$\nu(x) = \begin{cases} \alpha\omega\left(\dfrac{x - x_0}{\lambda}\right)^2, & for \quad |x_0| \le |x| \le |x_0| + \beta\lambda \\ 0, & for \quad |x| < |x_0| \end{cases} \tag{17}$$

where ω and λ mean the frequency and nonlinear wavelength of the incident wave respectively. The strength and the length of the damping zone are respectively controlled by two coefficients α and β. Based on the numerical tests in the presented problem, it is found that values of α and β can both be taken as 1.0. For initial condition at $t = 0$ in the mathematical modelling, the flap can be assumed to be put in the incident wave suddenly, and the potential on the free surface and the wave elevation can be taken as

$$\varphi(x, y = \eta, t = 0) = \varphi_{\mathrm{I},t=0}, \quad \eta(x, t = 0) = \eta_{\mathrm{I},t=0} \tag{18}$$

The mathematical problem is solved using the boundary element method. Through Green's identity, the Laplace equation in the fluid domain can be converted into an integral equation over its closed boundary S.

$$A(p)\varphi(p) = \int_S \left(G(p,q)\frac{\partial \varphi(q)}{\partial n_q} - \varphi(q)\frac{\partial G(p,q)}{\partial n_q} \right) dS_q \tag{19}$$

where $A(p)$ is the solid angle at the field point $p(x,y)$, while $q(x,y)$ denotes the source point, and the Green function can be written as

$$G(p,q) = \ln r_1 + \ln r_2 \tag{20}$$

with $r_1 = \sqrt{(x-x_0)^2 + (y-y_0)^2}$, $r_2 = \sqrt{(x-x_0)^2 + (y+y_0+2l)^2}$, and l being the vertical distance from the hinge centre to the bottom. The first term in Eq. (20) in fact corresponds to a source at point (x_0, y_0) while the second term is its mirror image about the bottom S_B at $y = -l$. Together they satisfy $\partial G / \partial \mathrm{n} = 0$ on S_B. Combining with Eq. (11), S_B then can be excluded from S in Eq. (19). The remaining boundary is divided into many small elements. Within each element the potential and its normal derivative are assumed to vary linearly. Boundary conditions are used, and the unknowns are then found from the solution of the matrix equation (Lu et al., 2000, Sun and Wu, 2013).

Once the solution of the above problem is found, the fluid moment may be obtained from the integration of the local moment created by the pressure over the flap surface. We have

$$M = -\int_{S_0(t)} (\varphi_t + \frac{1}{2}|\nabla\varphi|^2 + y - h)\cdot(xn_y - yn_x)dS + my_c \sin\gamma \tag{21}$$

where m is the mass of the flap and y_c is the vertical coordinate of the gravity centre of the flap when $\gamma = 0$. We note that in the equation, even when the velocity potential φ has been obtained at each time step numerically, φ_t is still not explicitly known. An effective method to resolve this is to treat φ_t as another unknown function which satisfies the Laplace equation in fluid domain. On the body surface, the normal derivative of φ_t can be written as (Wu, 1998)

$$\frac{\partial\varphi_t}{\partial n} = \dot{\Omega}\cdot(xn_y - yn_x) - \Omega\cdot\frac{\partial}{\partial n}(x\varphi_y - y\varphi_x) \tag{22}$$

We note that in the equation the acceleration $\dot{\Omega}$ is not yet known before Eq. (1) is solved, which in turn depends on M in Eq. (21) and $\dot{\Omega}$ in the Eq. (22). To decouple this nonlinear mutual dependence of the flap acceleration and fluid loading, we adopt the method of Wu and Eatock Taylor (1996, 2003). In particular, we define χ_1 and χ_2 as

$$\varphi_t = \dot{\Omega}\chi_1 + \chi_2 \tag{23}$$

They both satisfy the Laplace equation in the fluid domain. The body surface boundary conditions for χ_1 and χ_2 can respectively be written as

$$\frac{\partial\chi_1}{\partial n} = xn_y - yn_x, \quad \frac{\partial\chi_2}{\partial n} = -\Omega\cdot\frac{\partial}{\partial n}(x\varphi_y - y\varphi_x) \tag{24}$$

The second derivative in the normal direction can be transformed into that in the tangential directions

$$\frac{\partial \varphi_y}{\partial n} = \frac{\partial \varphi_x}{\partial l}, \quad \frac{\partial \varphi_x}{\partial n} = -\frac{\partial \varphi_y}{\partial l} \tag{25}$$

and their numerical calculations can be performed based on the procedure in Xu and Wu (2013). Based on the Bernoulli equation, together with zero pressure on the free surface, we have

$$\chi_1 = 0, \quad \chi_2 = -\frac{1}{2}\nabla\varphi \cdot \nabla\varphi - \eta \tag{26}$$

Sufficiently far away from the flap, φ_t tends to the temporal derivative of the incident wave potential φ_{It} after numerical damping is imposed in Eqs. (15) and (16). Thus the condition at the truncated boundary can be written as

$$\frac{\partial \chi_1}{\partial n} = 0, \quad \frac{\partial \chi_2}{\partial n} = \frac{\partial \varphi_{It}}{\partial n} \tag{27}$$

Based on χ_1 and χ_2, Eq. (21) can be written as

$$M = -\int_{S_0(t)} (\dot{\Omega}\chi_1 + \chi_2 + \frac{1}{2}\nabla\varphi \cdot \nabla\varphi + y - h) \cdot (xn_y - yn_x) dS + my_c \sin\gamma \tag{28}$$

If we define

$$a = \int_{S_0(t)} \chi_1 \cdot (xn_y - yn_x) dS \tag{29}$$

which is effectively an added inertia, and

$$M' = -\int_{S_0(t)} \left(\chi_2 + \frac{1}{2}\nabla\varphi \cdot \nabla\varphi + y - h \right) \cdot (xn_y - yn_x) dS + my_c \sin\gamma \tag{30}$$

Eq. (1) can be written as

$$(I + a_{\text{pto}} + a)\dot{\Omega} + b_{\text{pto}}\Omega + c_{\text{pto}}\gamma = M' \tag{31}$$

At $t = 0$, the free surface and the potential on the free surface are prescribed based on the incident wave, together with the initial value of γ and Ω. The solution of the discretized form of Eqs. (19) and (31) then gives $\dot{\Omega}$, from which Ω and γ can be updated though the Runge Kutta process. At the same time, Eqs. (12) and (13) are used to update the potential and free surface. The calculation then moves to the next time and it continues until the desired time step.

On the free surface the discrete element nodes may cluster or scatter in the process of updating, and thus the mesh needs to be re-generated after every few time steps. Here we choose the 5-point 4$^{\text{th}}$ order Lagrangian interpolation method to redistribute the nodes (Abramowitz and Stegun, 1964)

$$f(e) = \sum_{k=1}^{5} f_k l_k(e) \tag{32}$$

where

$$l_k(e)=\prod_{\substack{j=1\\ j\neq k}}^{5}\left(\frac{e-e_j}{e_k-e_j}\right) \tag{33}$$

is the Lagrangian interpolation polynomial. We adopt the length measured along the free surface as variable e, with its origin at the intersection between the free surface and body surface. e_j are the length coordinates of the nodes of the existing mesh and f_k is the value of function on node k. When the coordinate e of each new node after remeshing is obtained, Eq. (32) can then give (x,y,φ) at e.

The present methodology can deal with any given incoming wave. The tenth order and fifth order Stokes waves may give similar overall results in the present cases, such as total force and motion. When the detailed results such as higher order force components are needed, the higher order Stokes wave is more appropriate. Thus we choose the 10^{th} order periodic Stokes wave through Fourier approximation method (Fenton, 1988) as an example. The wave elevation and potential can be written as

$$\eta_{\mathrm{I}}=\frac{1}{k}\sum_{j=1}^{10}Y_j\cos(j\vartheta) \tag{34}$$

$$\varphi_{\mathrm{I}}=\frac{1}{\sqrt{k^3}}\sum_{j=1}^{10}B_j\frac{\cosh\left[jk(d+y-h)\right]}{\cosh(jkd)}\sin(j\vartheta) \tag{35}$$

where

$$\vartheta=k(x-ct)+\vartheta_0 \tag{36}$$

and ϑ_0 is the initial phase, k is the wave number and c is the wave velocity. The detailed results for B_j, Y_j can be obtained through a set of nonlinear equations (Fenton, 1988). All the parameters above are nondimensionalized based on the manner described before Eq. (1).

2.3 Linear frequency domain method for fluid flow

When the wave amplitude and motion amplitude are small, the problem can be simplified as a linear one. We may follow the analysis in Section 7.9.2 of (Mei, 1983). M in Eq. (1) can be decomposed as the hydrodynamic moments due to the incident wave M_{i} and diffracted wave M_{e}, the radiated wave M_{r}, the buoyancy M_{b} and the weight of the flap M_{g}

$$M=M_{\mathrm{i}}+M_{\mathrm{e}}+M_{\mathrm{r}}+M_{\mathrm{b}}+M_{\mathrm{g}} \tag{37}$$

The last two terms are related to the displacement γ and therefore together they constitute the restoring moment. The boundary conditions will be imposed at the mean position of each surface and only linear terms will be retained. Correspondingly there will be only the first term of $n=1$ in Eq. (3). Also only the linear term in Eq. (35) is used for the incident potential, which can be

written as

$$\varphi_{\mathrm{I}} = \mathrm{Re}(A\varphi_{\mathrm{i}} e^{-i\omega t}) \tag{38}$$

where A is the linear wave amplitude and $\varphi_i = -\frac{i}{\omega}\frac{\cosh[k(\eta_{\mathrm{I}}+d)]}{\cosh(kd)}e^{ikx}$. The total potential can be decomposed as

$$\varphi = \mathrm{Re}[(-i\omega\theta_1\varphi_{\mathrm{r}} + A\varphi_{\mathrm{d}} + A\varphi_{\mathrm{i}})e^{-i\omega t}] \tag{39}$$

where φ_{r} and φ_{d} are respectively wave radiation and diffraction potentials, and they satisfy the following body surface boundary conditions

$$\frac{\partial\varphi_{\mathrm{r}}}{\partial n} = xn_y - yn_x \tag{40}$$

$$\frac{\partial\varphi_{\mathrm{d}}}{\partial n} = -\frac{\partial\varphi_{\mathrm{i}}}{\partial n} \tag{41}$$

Their contributions to the moment can be written in the following forms

$$-a_{\mathrm{z}}\theta_1\omega^2 - b_{\mathrm{z}}\theta_1 i\omega = (i\omega)^2\theta_1\int_{S_0}\varphi_{\mathrm{r}}(xn_y - yn_x)dS \tag{42}$$

$$M'' = iA\omega\int_{S_0}(\varphi_{\mathrm{d}} + \varphi_{\mathrm{i}})\cdot(xn_y - yn_x)dS \tag{43}$$

$$-c_{\mathrm{z}}\theta_1 = -(m_{\mathrm{b}}y_{\mathrm{b}} - my_{\mathrm{c}})\theta_1 \tag{44}$$

where m_{b} is the mass of the water displaced by the flap at the vertical position, y_{b} is the vertical coordinate of the buoyancy centre and $\sin\gamma \approx \gamma$ has been used due to linearization. Eq. (1) can then be transformed as

$$|\theta_1| = \frac{|M''|}{\sqrt{[(I + a_{\mathrm{pto}} + a_{\mathrm{z}})\cdot\omega^2 - (c_{\mathrm{pto}} + c_{\mathrm{z}})]^2 + \omega^2(b_{\mathrm{pto}} + b_{\mathrm{z}})^2}} \tag{45}$$

a_{z} and b_{z} here respectively are effectively the linear added inertia and radiation damping coefficient, and they are both the function of the frequency ω. c_{z} is the restoring force coefficient due to the difference in the contributions from the hydrostatic term and the weight of the flap. From Eq. (45), Eq. (4) becomes

$$E_{\mathrm{P}} = \frac{1}{2}\frac{b_{\mathrm{pto}}|M''|^2}{[(I + a_{\mathrm{pto}} + a_{\mathrm{z}})\omega - (c_{\mathrm{pto}} + c_{\mathrm{z}})/\omega]^2 + (b_{\mathrm{pto}} + b_{\mathrm{z}})^2} \tag{46}$$

For the linear problem and a symmetric body, the Haskind relationship (Mei, 1983)

$$\left|M''\right|^2 = 2A^2 C_g b_z \tag{47}$$

may be used, where C_g is the group velocity. Eq. (46) becomes

$$E_P = \frac{b_{pto} b_z A^2 C_g}{[(I + a_{pto} + a_z)\omega - (c_{pto} + c_z)/\omega]^2 + (b_{pto} + b_z)^2} \tag{48}$$

For the linear wave, Eq. (6) gives

$$E_W = \frac{1}{2} A^2 C_g \tag{49}$$

Thus the efficiency in Eq. (7) becomes

$$R = \frac{2 b_{pto} b_z}{[(I + a_{pto} + a_z)\omega - (c_{pto} + c_z)/\omega]^2 + (b_{pto} + b_z)^2} \tag{50}$$

To find the added inertia a_z and radiation damping coefficient b_z through our present time stepping method, we can impose the flap in the forced rotation in calm water with a small amplitude γ_0, or

$$\gamma = \gamma_0 \sin \omega t \tag{51}$$

When the numerical result becomes virtually periodic, the temporal variation of the moment M_r can be written as

$$M_r = -a_z \gamma_0 \omega^2 \sin(\omega t) + b_z \gamma_0 \omega \cos(\omega t) \tag{52}$$

from which a_z and b_z can be obtained based on the variation of M_r with time. The natural frequency ω_n is defined when the inertial term is cancelled by the restoring force, and can therefore be obtained from

$$\omega_n = \sqrt{\frac{c_{pto} + c_z}{I + a_{pto} + a_z}} \tag{53}$$

Based on Eq. (46), in a given incident wave of fixed ω, the extracted power for the flap can be optimized by adjusting

$$b_{pto} = b_{opt} = \sqrt{\frac{((I + a_{pto} + a_z)\omega^2 - (c_{pto} + c_z))^2}{\omega^2} + b_z^2} \tag{54}$$

which is obtained by using $\frac{\partial E_P}{\partial b_{pto}} = 0$. Substituting this into Eq. (46), we have

$$E_P = \frac{1}{4} \cdot \frac{b_{opt} \left|M''\right|^2}{b_{opt}^2 + b_z^2} \tag{55}$$

Eq. (55) means that at a given wave frequency, when b_{pto} is chosen based on Eq. (54) for a given device, E_P will achieve its maximum. We then notice that based on such a choice we have

$b_{\text{opt}} \geq b_{\text{z}}$ and its lowest value $b_{\text{opt}} = b_{\text{z}}$ is achieved when the $\omega_{\text{n}} = \omega$. We also notice when $b_{\text{opt}} = b_{\text{z}}$, Eq. (55) reaches its highest value at

$$E_{\text{P}} = \frac{1}{4} A^2 C_{\text{g}} \tag{56}$$

which is the same as that of Eq. (9. 10) of Section 7.9.2 of (Mei, 1983). Substituting Eqs. (49) and (56) into (7), we notice that the highest efficiency is 50%. This is a well known result for a symmetric device based on the linear theory and will be assessed below when the nonlinear theory is used.

3. Numerical results and discussions

3.1 Convergence study and validation

The computational domain is truncated at $|x| = 6\lambda$ where λ is the nonlinear wavelength. The smallest elements of length l_{m} are used on the body surface and on the free surface nearer to the body, for example up to $|x| = 1$. Beyond this point, the size of the element increases gradually at a fixed ratio δ. However it is limited by a maximum of $\lambda / 25$. The time step Δt, is taken as a fraction of the ratio of $l_{\text{m}} / (\mu V_{\text{max}})$, where V_{max} is the maximum of the velocity magnitude on the free surface at each time step and $\mu > 1$ is a coefficient. Simultaneously, Δt is not allowed to be larger than $\Delta t_{\text{m}} = T / n$, or at least n time steps are needed within one period. The angular displacement history with three different meshes and two different time steps are shown in Figs. 2 and 3 respectively. The height of the flap h, thickness B, rotational inertia about the hinge I, mass m and the height of mass centre y_{c} in Fig. 1 are respectively set as 1.0, 0.427, 0.063, 0.153 and 0.646. The frequency and height of the incident wave are respectively set as $\omega = 0.478$ and $H = 0.49$. Water depth $d = 1.49$. Mechanical coefficients of the converter a_{pto}, b_{pto} and c_{pto} are all set as 0. The good agreement can be seen in the figures and this verifies that the present method is mesh and time independent. Unless specified, in the following simulations, $l_{\text{m}} = 0.1$, $\delta = 1.01$, $\mu = 5$ and $n = 100$. The main parameters for the oscillating wave surge converter in Figs. 2 and 3 are adopted in the following simulations, unless their variations are specifically explained.

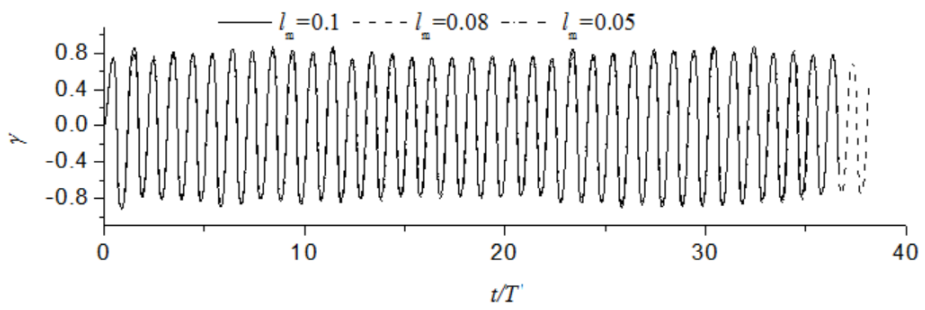

Fig. 2. Mesh convergence study

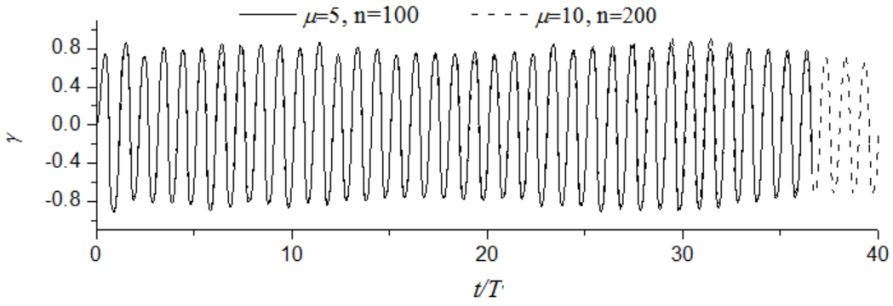

Fig. 3. Time step convergence study

We now consider the case in Henry et al. (2014) for comparison. $h = 0.205\text{m}$ is the height of the flap in Fig. 1 in dimensional sense. The motion is excited by a wave with height $H = 0.1\text{m}$ and period $T = 1.9\text{s}$, and the water depth d is set as 0.305m. The thickness B, rotational inertia about the hinge I, mass m and the height of mass centre y_c are respectively set as 0.0875m, 0.1147kgm^2, 4.27kg and 0.1324m. After nondimensionalization, the values of H, T, d, h, B, I, m and y_c are the same as those in Figs. 2 and 3. The coefficient a_{pto}, b_{pto} and c_{pto} due to mechanical system are all set as zero. The histories of the angular displacement and velocity from the present fully nonlinear BEM are presented in Fig. 4. The tip of the jet was cut regularly (Sun et al., 2015). The results are compared with the experimental data of Henry et al. (2014) and those from their numerical simulation based on the finite volume approach through Fluent Software. Dimensional parameters are used in the figure to be consistent with their results. It can be seen from the figures that all the results are in good agreement in general, while the present results are even closer to the experimental data. This validates the present methodology and procedure.

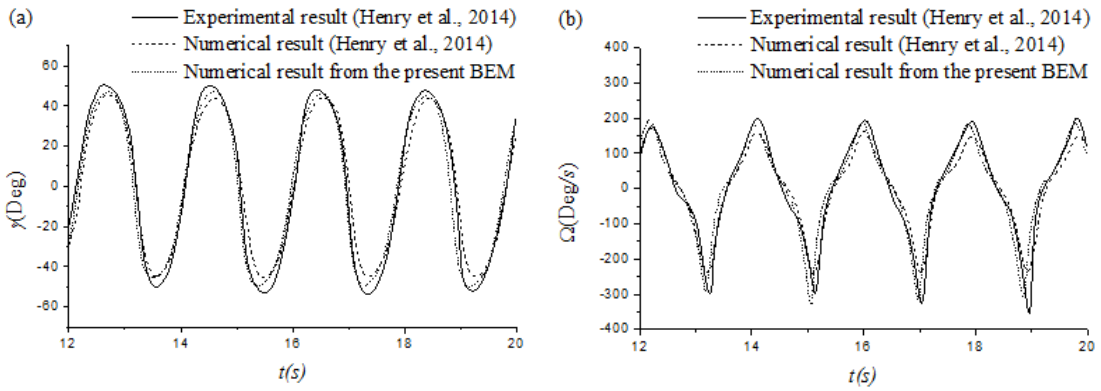

Fig. 4. Comparison between the present result and those of Henry et al. (2014) (a) the angular displacement γ and (b) the angular velocity Ω.

3.2 The effect of the design parameters for the generator

We now investigate how the variation of the coefficients a_{pto}, b_{pto} and c_{pto} will affect the results under a given wave. The frequency ω of the incident wave will be set as 0.5. At this frequency, the added inertia a_z is approximately 0.739 and the radiation damping coefficient b_z

is about 0.336 from the linear theory. Based on Eqs. (54) and (55), when b_{pto} is set as b_{opt}, the rate of extracted power E_{P} can reach its peak. In such a case when natural frequency ω_{n} is close to the wave frequency ω, E_{P} can reach the highest value. To investigate such a behaviour, the flap is released into a wave with height $H = 0.05$, which is small enough that nonlinear characteristics will not have major effect on the results. Fig. 5 gives the motion amplitude γ_0 and the rate of power extracted E_{P} against ω_{n} at different b_{pto}. E_{P} is calculated from Eq. (2) when the results become virtually periodic, for example at $t > 20T$, and the number of periods m are taken as 20 or more. γ_0 is measured from the mean peak value during the m periods. According to Eq. (53), ω_{n} can be adjusted by changing a_{pto} or c_{pto}, and the effects will be similar. In the current case, c_{pto} is adjusted to vary ω_{n} around ω while $a_{\text{pto}} = 0$. b_{pto} is set as νb_{opt}, where ν is a coefficient. Fig. 5 give the results for ν=0, 0.5, 1.0 and 1.5 respectively. As expected at $\nu = 0$, or when the mechanical damping is zero, the motion amplitude γ_0 is largest. However, this large motion does not lead to any energy extraction by the flap. In fact we have $E_{\text{P}} = 0$ at $\nu = 0$ based on the Eq. (2). This means that all the energy has been returned to wave. To absorb energy, ν must be larger than 0. It can be seen when $\nu = 0.5$, the motion amplitude becomes smaller due to the additional damping. However, exactly due to the reduced motion, some of the energy has been transferred to the generator, which can be seen through the curve of E_{P} in Fig. 5(b). Based on the linear theory, when b_{pto} is given by Eq. (54), E_{P} will reach its optimum at each ω_{n}. This can be seen from the curve of E_{P} at $\nu = 1$, which is higher than the curve of $\nu = 0.5$ as well as the curve of $\nu = 1.5$. The motion amplitude γ_0 on the other hand always decreases as ν increases. This shows that at motion of either very large amplitude or very small amplitude, corresponding to the small and large mechanical damping respectively, the rate of power extracted E_{P} is small. The largest E_{P} occurs at motion with middle range amplitude when $b_{\text{pto}} = b_{\text{opt}}$. At each given ν, however, both γ_0 and E_{P} will reach their maximum at $\omega_{\text{n}} \approx \omega$, or when resonance occurs. Thus overall E_{P} is the largest when $\omega_{\text{n}} \approx \omega$ and $b_{\text{pto}} = b_{\text{opt}}$, which is consistent with the discussion in Sec. 2.3.

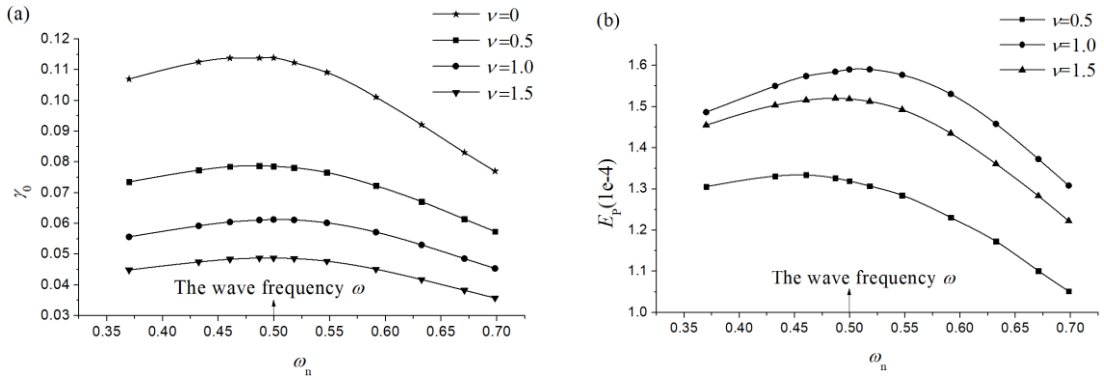

Fig. 5. Results against ω_n at different b_{pto} ($H = 0.05$, $a_{pto} = 0$, $\omega = 0.5$) (a) the motion amplitude of the flap γ_0 and (b) the rate of power extracted E_P

We now consider the effect of the wave height H. In the linear theory, γ_0 is linearly proportional to H, while E_P to H^2. The efficiency R is independent of H.The results for γ_0 / H, E_P / H^2 and the efficiency R against ω_n with different H are provided in Fig. 6. All the curves for motion amplitude in Fig. 6(a) reach their peaks when $\omega_n \approx \omega$. However, this is not exactly true in Figs. 6(b) for the extracted power and (c) for efficiency. When H is small, for example at $H = 0.05$, the results are very close to those from the linear theory, and the peak E_P and R both appear at $\omega_n \approx \omega$. The largest difference between the result of $H = 0.05$ and that of linear theory is no more than 3%. The peak happens when ω_n may be slightly larger than 0.5, but the difference is no more than 1%. When H is increased to 0.2, E_P / H^2 and R become slightly larger. The largest E_P / H^2 and R also appear at $\omega_n \approx \omega$. When H is increased to 0.5, nonlinear effect becomes far more prominent, and some very different features appear. When ω_n is small, both γ_0 / H and E_P / H^2 at $H = 0.5$ are smaller than those at $H = 0.05$ and $H = 0.2$. However E_P at $H = 0.5$ increases much faster with ω_n. It becomes much bigger than those at $H = 0.05$ and 0.2 at large ω_n. Its peak occurs when ω_n is away from ω. We may notice that the natural frequency ω_n is estimated from the linear theory. At large H, the real ω_n will be affected by the nonlinearity obviously. At a given ω and H, E_W will be a constant. Thus based on Eq. (6), the efficiency curves in Fig. 6(c) follow the exact shapes of the corresponding E_P curves in Fig. 6(b). However E_W at different H is different, therefore the relative

magnitudes of those at $H = 0.05$, 0.2, 0.5 in Figs. 6(b, c) are different. Based on the discussion after Eq. (56), the highest possible efficiency from the linear theory is 50%. This can be observed from Fig. 6(c) at $H = 0.05$. However, at larger H, this barrier can be broken and the efficiency can exceed this limit.

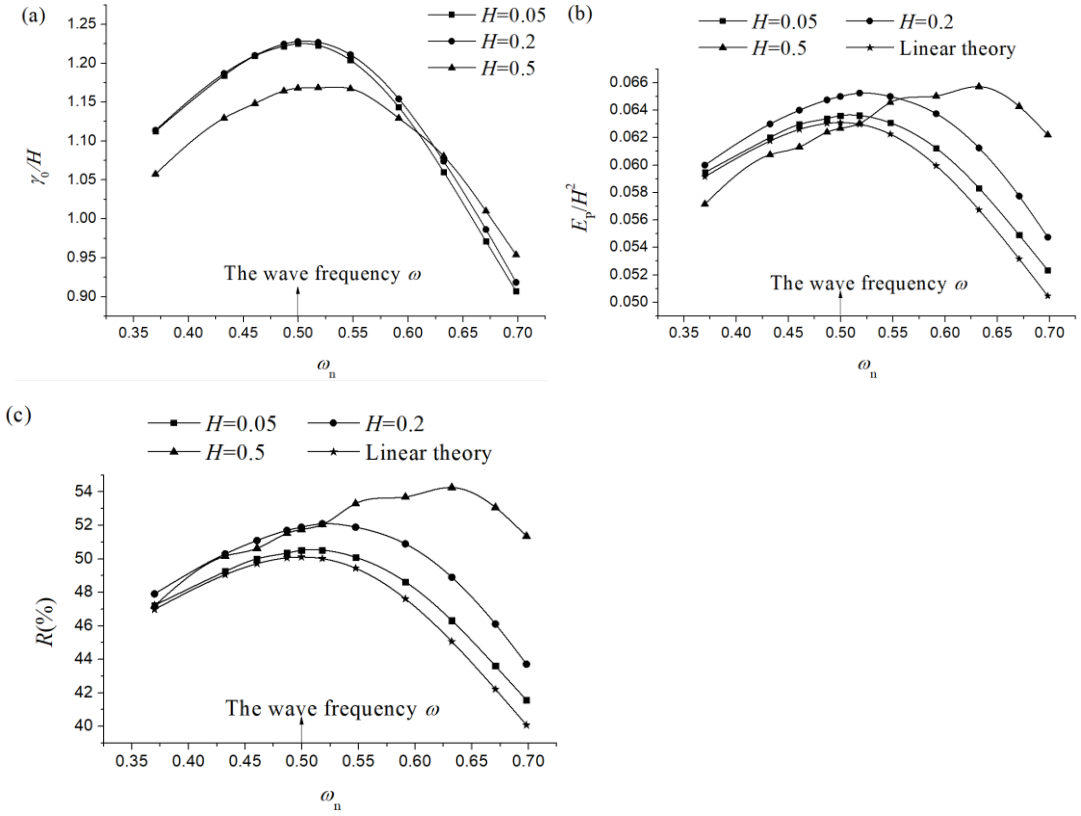

Fig. 6. Results against ω_n at different H ($a_{pto} = 0$, $b_{pto} = b_{opt}$, $\omega = 0.5$) (a) γ_0 / H, (b) E_p / H^2 and (c) R

3.3 Behaviour of an oscillating wave surge converter in different incident waves

We then consider the cases in which an oscillating wave surge converter with fixed mechanical properties is in different waves. When mechanical coefficient a_{pto} and c_{pto} are both set as zero, the natural frequency of the flap is 0.324, and this corresponds to a radiation damping coefficient $b_z = 0.166$. Thus mechanical damping coefficient b_{pto} is set as 0.166. The wave frequencies chosen in current case correspond fully to the range in the experiment of Henry et al. (2014). γ_0 / H, E_p / H^2 and R against ω with different H are provided in Fig. 7. As ω increases, both γ_0 / H and E_p / H^2 decrease gradually, and efficiency R decreases first and becomes more stable later. When $H = 0.05$ and 0.2, nonlinear effect on γ_0 and E_p is not prominent, and the results are close to those of linear theory. The nonlinear effect becomes

prominent at $H = 0.5$. γ_0 / H and E_p / H^2 are lower when $\omega < 0.8$, while R is lower over the whole range of the frequency.

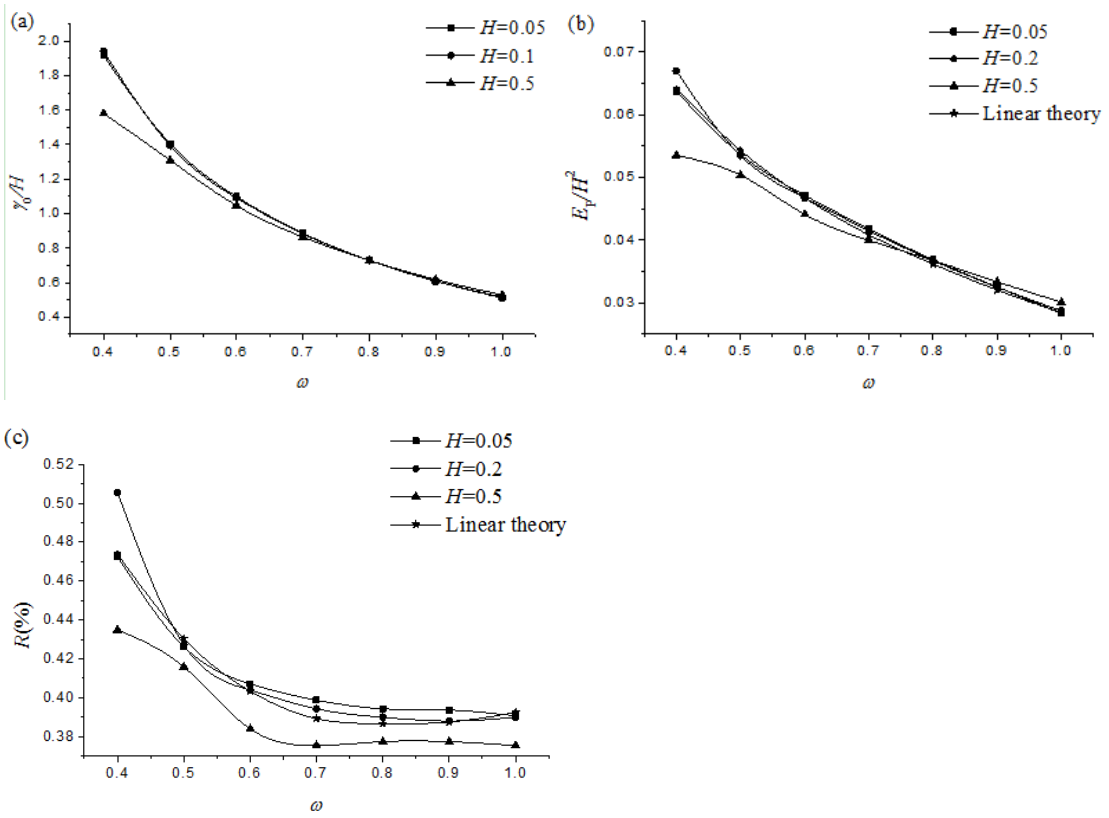

Fig. 7. Results against ω at different H ($a_{pto} = 0$, $b_{pto} = 0.166$, $c_{pto} = 0$) (a) γ_0 / H, (b) E_p / H^2 and (c) R

In the above case, the frequencies of incident waves are all larger than natural frequency ω_n and there is no peak in Fig. 7. We now adjust the natural frequency ω_n to 0.5, which can be achieved by setting $c_{pto} = 0.091$ and $a_{pto} = 0$. The mechanical damping coefficient is set as $b_{pto} = 0.336$, which corresponds to the radiation damping coefficient b_z at $\omega = 0.5$, or is the optimal b_{opt} when $\omega_n = \omega$. Figs. 8 (a, b, c) give the ratio of γ_0 / H, the ratio of E_p / H^2 and the efficiency R respectively against wave frequency ω. It is interesting to see as ω increases, γ_0 / H decreases and there is no peak at $\omega_n = \omega$. This is because the damping term in Eq. (45) is relatively large compared with the difference of inertial and restoring force terms. Thus even when the difference is zero, i.e, when $\omega_n = \omega$, the ratio of γ_0 / H is not the prominently largest.

Also unlike results in Fig. 6 where the excitation force $|M''|$ in Eq. (46) does not vary with ω_n, it varies here with ω. For the same reason, there is no obvious peak of E_P in Fig. 8(b) either. However the peak is obvious for the efficiency in Fig. 8(c). The figure shows that when the mechanical properties of the converter are tuned for a given wave frequency, the device can achieve the highest efficiency at this frequency. However, when the incoming wave changes, the efficiency can decrease significantly, especially if the wave amplitude is large. This suggests that when a device is designed, a balance may need to be found if the wave condition at the site changes regularly.

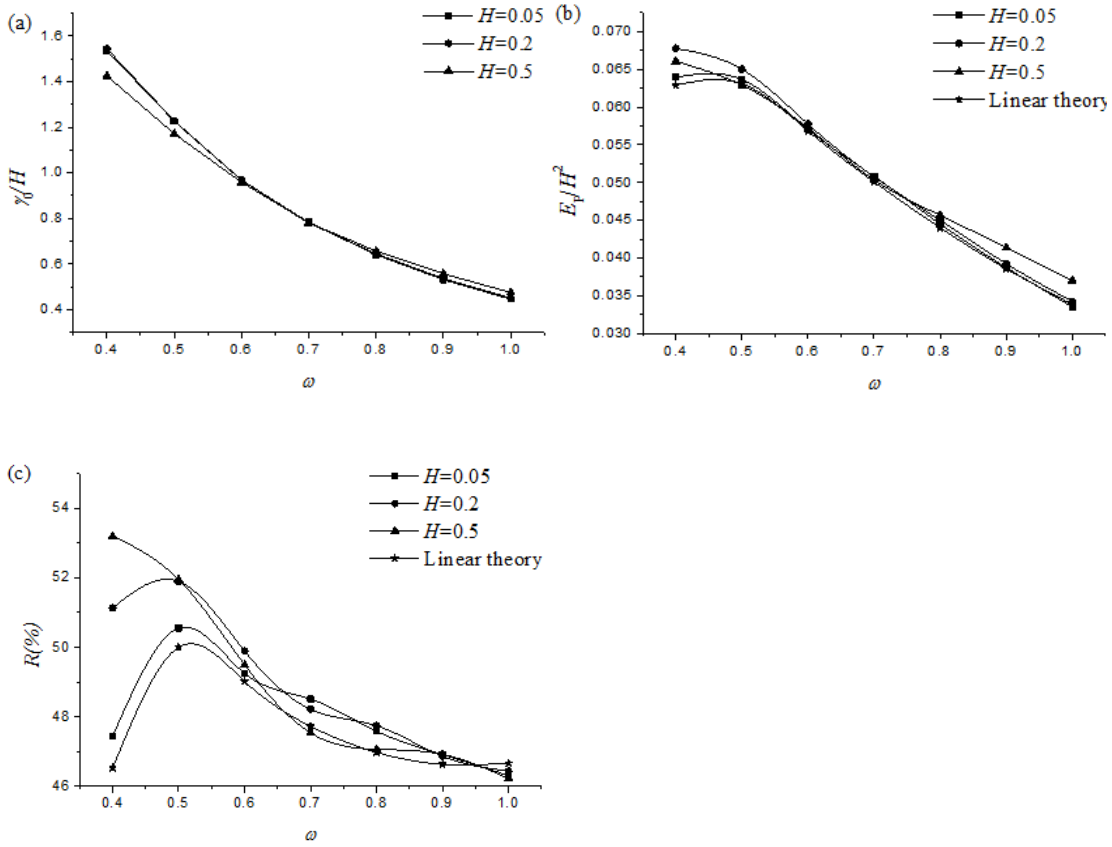

Fig. 8. Results against ω at different H ($a_{pto}=0$, $b_{pto}=0.336$ and $c_{pto}=0.091$) (a) the ratio of γ_0 / H, (b) the ratio of E_P / H^2 and (c) the efficiency R.

4. Conclusions

The performance of the oscillating wave surge converter has been analysed based on the fully nonlinear velocity potential theory with the boundary element method. The following conclusions can be made.

(1) The choice of the mechanical damping b_{pto} of the converter is highly significant for an optimal extraction of wave power. Based on the linear theory the wave energy converter will achieve the highest possible efficiency of 50% when $b_{pto}=b_{opt}$. However this limit can be exceeded when the

nonlinear theory is used.

(2) For the wave at a given frequency, the mechanical parameters of devices can be adjusted to improve the efficiency. At a small wave amplitude, the high efficiency is reached when the natural frequency is equal to the wave frequency. However it is no longer the case when the wave amplitude is large and nonlinear effect is important.
(3) In the design of an OWSC, the natural frequency can be tuned to the characteristic frequency of the wave to achieve the high efficiency. However this may mean much lower efficiency when the sea-state changes. Therefore it is important to ensure the wave energy converter is efficient in a band of frequencies of a range of incoming waves.

Acknowledgements

This work is supported by Lloyd's Register Foundation through the joint centre involving University College London, Shanghai Jiaotong University and Harbin Engineering University, to which the authors are most grateful. Lloyd's Register Foundation helps to protect life and property by supporting engineering-related education, public engagement and the application of research.

This work is also supported by the National Natural Science Foundation of China (Grants No. 11472088).

References

Abramowitz, M. and Stegun, I.A., 1964. Handbook of mathematical functions with formulas, graphs, and mathematical tables, U.S. Government Printing Office, Washington DC.

Aliabadi, F.H., Ghadimi, P., Djeddi, S.R. and Dashtimanesh, A., 2013. 2-D numerical wave tank by boundary element method using different numerical techniques, Global Journal of Mechanics and Analysis, 1, 11-21.

Budal, K. and Falnes, J., 1975. A resonant point absorber of ocean-wave power, Nature, 256, 478–479.

Budal, K. and Falnes, J., 1978. Wave-power conversion by point absorbers, Norwegian Maritime Research, 6, 2–11.

Contento, G., Codiglia, R. and D'Este, F., 2001. Nonlinear effects in 2D transient nonbreaking waves in a closed flume, Applied Ocean Research, 23, 3–13.

Crowley, S., Porter, R. and Evans, D.V., 2013. A submerged cylinder wave energy converter, Journal of Fluid and Mechanics, 716, 566-596.

Evans, D.V., 1976. A theory for wave-power absorption by oscillating bodies, Journal of Fluid and Mechanics, 77, 1-25.

Evans, D.V., 1981. Maximum wave-power absorption under motion constraints, Applied Ocean Research, 3, 200–203.

Eriksson, M., Isberg, J. and Leijon, M., 2005. Hydrodynamic modelling of a direct drive wave energy converter, International Journal of Engineering Science, 43, 1377-1387.

Evans, D.V. and Porter, R., 2012. Wave energy extraction by coupled resonant absorbers, Philosophical Transactions of the Royal Society A, 370, 315-344.

Fenton, J.D., 1988. The numerical solution of steady water wave problems, Computers & Geosciences, 14, 357-68.

Folley, M., Whittaker, T. and Henry, A., 2005. The performance of a wave energy converter in shallow water, Sixth European Wave and Tidal Energy Conference, Glasgow.

Folley, M., Whittaker, T.J.T. and Henry, A., 2007a. The effect of water depth on the performance of a small surging wave energy converter, Ocean Engineering, 34, 1265-1274.

Folley, M., Whittaker, T.J.T. and van't Hoff, J., 2007b. The design of small seabed- mounted bottom hinged wave energy converters, Proceedings of the Seventh European Wave and Tidal Energy Conference, Porto, Portugal.

Folley, M., and Whittaker, T.J.T., 2009. Analysis of the nearshore wave energy resource, Renewable Energy, 34, 1709-1715.

Folley, M., Elsaesser, B. and Whittaker, T., 2009. Analysis of the wave energy resource at the European Marine Energy Centre, In Coasts, Marine Structures and Breakwaters Conference, Edinburgh, UK.

Henry, A., Kimmoun, O., Nicholson, J., Dupont, G., Wei, Y. and Dias, F., 2014. A two dimensional experimental investigation of slamming of an oscillating wave surge converter, Proceedings of the twenty-fourth International Ocean and Polar Engineering conference, Busan, Korea.

Lighthill, J., 1978. Waves in Fluids, Cambridge University Press, Cambridge.

Lu, C.H., He, Y.S. and Wu, G.X., 2000. Coupled analysis of nonlinear intersection between fluid and structure during impact, Journal of Fluids and Structures, 14, 127-146.

Mei, C.C., 1983. The applied dynamics of Ocean surface waves, World Scientific Publishing Co Pte Ltd, Singapore.

Mei, C.C., 2012. Hydrodynamic principles of wave power extraction, Philosophical Transactions of the Royal Society A, 370, 208-234.

Renzi, E. and Dias, F., 2012a. Resonant behaviour of an oscillating wave energy converter in a channel, Journal of Fluid and Mechanics, 701, 482-510.

Renzi, E. and Dias, F., 2012b. Relations for a periodic array of flap-type wave energy converters, Applied Ocean Research, 39, 31-39.

Renzi, E. and Dias, F., 2013. Hydrodynamics of the oscillating wave surge converter in the open ocean, European Journal of Mechanics- B/Fluids, 41, 1-10.

Rafiee, A., Elsaesser, B. and Dias, F., 2013. Numerical simulation of wave interaction with an oscillating wave surge converter, Proceedings of the ASME 32nd International Conference on Ocean, Offshore and Arctic Engineering, Nantes, France.

Salter, S., 1974. Wave power, Nature, 249, 720–724.

Sarkar, D., Doherty, K., Dias, F., 2016. The modular concept of the Oscillating Wave Surge Converter. Renewable Energy, 85, 484-497.

Sun, S.L., Wu, G.X, 2013. Oblique water entry of a cone by a fully three dimensional nonlinear method, Journal of Fluids and Structures, 42, 313-32.

Sun, S.Y., Sun, S.L., Ren, H.L. and Wu, G.X., 2015. Splash jet and slamming generated by a rotating flap, Physics of Fluids, 27, 092107.

Schmitt, P. and Elsaesser, B., 2015. On the use of OpenFOAM to model oscillating wave surge converters, Ocean Engineering, 108, 98-104.

Van't Hoff, J., 2009. Hydrodynamic modelling of the oscillating wave surge converter, PhD thesis, Queen's University, Belfast.

Wehausen, J.V. and Laitone, E.V., 1960. Surface Waves. Encyclopaedia of Physics (Springer Verlag), 9, 446–778.

Wilkinson, L., Whittaker T.J.T., Thiesc, P.R., Dayd, S., Ingrame, D., 2017. The power-capture of a nearshore, modular, flap-type wave energy converter in regular waves. Ocean Engineering, 137,

394-403.

Wu, G.X. and Eatock Taylor, R., 1996. Transient motion of a floating body in steep waves, 11th Workshop on Water Waves and Floating Bodies, Hamburg, Germany.

Wu, G.X., 1998. Hydrodynamic force on a rigid body during impact with liquid, Journal of Fluids and Structures, 12, 549-59.

Wu, G.X. and Eatock Taylor, R., 2003. The coupled finite element and boundary element analysis of nonlinear interactions between waves and bodies, Ocean Engineering, 30, 387-400.

Whittaker, T. and Folley, M., 2012. Nearshore oscillating wave surge converters and the development of Oyster, Philosophical Transactions of the Royal Society A, 370, 345-364.

Wei, Y., Rafiee, A., Henry, A. and Dias, F., 2015. Wave interaction with an oscillating wave surge converter, Part I: Viscous effects, Ocean Engineering, 104, 185-203.

Wei, Y., Abadie, T., Henry, A. and Dias, F., 2016. Wave interaction with an Oscillating Wave Surge Converter, Part II: Slamming, Ocean Engineering, 113, 319-334.

Xu, G.D. and Wu, G.X., 2013. Hydrodynamics of a submerged hydrofoil advancing in waves, Applied Ocean Research, 42, 70–78.

Yeylaghi, S., Moa, B., Oshkai, P., Buckham, B., Crawford, C., 2016. ISPH modelling of an oscillating wave surge converter using an OpenMP-based parallel approach. Journal of Ocean Engineering and Marine Energy, 2, 301-302.